

Contents lists available at ScienceDirect

# Acta Materialia

journal homepage: www.elsevier.com/locate/actamat



# Full length article

# Evaluation of a modified void descriptor function to uniquely characterize pore networks and predict fracture-related properties in additively manufactured metals



Dillon S. Watring<sup>a,\*</sup>, Jake T. Benzing<sup>b</sup>, Orion L. Kafka<sup>b</sup>, Li-Anne Liew<sup>b</sup>, Newell H. Moser<sup>b</sup>, John Erickson<sup>a</sup>, Nikolas Hrabe<sup>b</sup>, Ashley D. Spear<sup>a</sup>

- <sup>a</sup> Department of Mechanical Engineering, University of Utah, Salt Lake City, UT, USA
- <sup>b</sup> National Institute of Standards and Technology (NIST), Boulder, CO, USA

# ARTICLE INFO

# Article history: Received 22 June 2021 Revised 29 October 2021 Accepted 2 November 2021 Available online 3 November 2021

Keywords: Inconel 718 Laser powder bed fusion Ductile fracture X-Ray computed tomography Porosity

#### ABSTRACT

Subtle differences among additive manufacturing (AM) processing parameters lead to variations in pore networks and complicate the prediction of void-sensitive mechanical behaviors, including location of fracture. The current work expands upon a recently developed pore metric, the void descriptor function (VDF), by accounting for interactions among neighboring pores and stress concentrations induced by nonspherical pores or voids. The modified VDF is evaluated against 120 computationally generated fracture simulations and six physical tensile specimens of as-built laser powder bed fused IN718. The latter set of experiments, which include X-ray computed tomography measurements before and after deformation, enables evaluation against pore populations that are representative of defects commonly observed in AM metals. The modified VDF accurately predicts fracture location (within  $\pm 5\%$  tolerance) for 94 out of 120 simulated specimens, representing 3.3%, 62.1%, and 59.3% increases in the number of accurate predictions in comparison to predictions based on the original VDF, the location of maximum cross-sectional area reduction, and the largest-pore location, respectively. In the experimental data set, the modified VDF accurately predicts the location of fracture in five out of six specimens compared to only two out of six using the original VDF, maximum cross-sectional area reduction, or largest-pore location. Also, the maximum value of the modified VDF was found to be more highly correlated than fraction porosity, pore size, reduced-cross section area, and total number of pores to the ultimate tensile strength, elongation to failure, and toughness modulus, suggesting that the modified VDF presented in this work could serve as a promising metric to assist with characterizing unique pore networks and predicting fracture-related properties in AM components.

© 2021 Acta Materialia Inc. Published by Elsevier Ltd. All rights reserved.

## 1. Introduction

Metal additive manufacturing (AM) has become a popular and vital manufacturing tool in a variety of industries [1–3]. There are many benefits of AM techniques over traditional manufacturing, including the ability to achieve high accuracy in fine details, reduced manufacturing time, and geometric flexibility [4]. There has been a significant amount of work investigating the relationship among the microstructure and tensile properties in AM metals, which vary widely from under-performing to over-performing when mechanical properties are compared against wrought or cast metals [5–10]. However, recent works have begun to acknowledge the im-

portant role that defects in general, and pores in particular, play in the mechanical response of AM metals [5,11–13]. The complexity of pore structures can, in part, be attributed to the different types of pores that exist in AM metals: gas pores, keyhole pores, and lack-of-fusion pores [14]. These different types of pores have variable mechanisms of formation as well as variability in their respective impact on the mechanical response [15–23]. For example, Hilaire et al. [24] showed that lack-of-fusion pores (irregularly shaped) created localized stress concentrations and promoted the initiation of sharp cracks more often than did spherical (gas and keyhole) pores. Pores have also been shown to be one of the main drivers in poor fatigue performance in AM metals [12,19]. Many of these works highlight the importance of understanding the unique formation of pores and their corresponding impact on fracture-related properties in AM metals.

<sup>\*</sup> Corresponding author. E-mail address: dillon.watring@utah.edu (D.S. Watring).

In ductile metals specifically, one of the most important failure mechanisms is void coalescence and growth, further highlighting the importance of pores and pore structures [25]. Many models have been developed in an attempt to understand the impact of pores on the mechanical response in metals [26-30]. However, most of these models make many assumptions when predicting the mechanical properties. One important assumption these models make is that pore networks are homogeneously distributed throughout the material. Since realistic pore networks are likely inhomogeneously distributed, especially in AM metals, these models are unable to properly capture the relationship between pore structures and mechanical response. However, with the emergence of high-resolution X-ray computed tomography (CT), the measurement of exact size, shape, and location of individual pores has made modeling the impact of inhomogeneous pore networks on mechanical properties feasible.

Recently, an advanced multiscale model method was proposed to capture the impact of inhomogeneous distributions of pores on fatigue and fracture behavior [31]; while the method captures pore size, shape, and location using images of pores from X-ray CT, the model is computationally expensive and requires a highly skilled operator to use effectively. To avoid the complexity of directly performing pore-resolved numerical simulations, geometric pore parameters have been used as a way of characterizing pore structures and using such metrics to predict or correlate with the mechanical response [32]. In one example, Du Plessis et al. [33] showed that for cast Ti-6Al-4V tensile specimens imaged using X-ray CT, the fracture location corresponded to the location of the largest measured pore in some, but not all, of the cases investigated. There have been other examples reported in the literature indicating that the location of the largest pore does not generally correspond to fracture location or tensile behavior. For example, Madison et al. [34] characterized AM stainless steel 17-4PH tensile specimens using a variety of pore metrics and attempted to correlate them to the mechanical response. They showed that common pore metrics, such as maximum reduction of cross-sectional area, total pore volume, maximum pore volume, and the number of pores, had no strong correlation with the measured tensile properties, namely yield strength. The apparent lack of correlation suggests that other factors besides porosity play a key role in the fracture of AM metals, or that the current pore metrics inadequately characterize pore networks for the purposes of predicting mechanical response.

A significant advance in the characterization of pore networks was recently presented by Erickson et al. [35], in which a new pore metric, called the void descriptor function (VDF), was derived to uniquely characterize networks of spherical pores in metals. The VDF metric was derived to account for pore clustering (relative to a location along the gauge length), pore sizes, and pore locations relative to the nearest free surface of the specimen. Erickson et al. [35] then compared the capabilities of the VDF and other commonly used pore metrics to predict fracture locations for 120 simulated fracture tests. They showed that the location of the maximum VDF value corresponded with the actual fracture location (within  $\pm 5\%$  of the total gauge length) in 91 out of 120 (76.0%) specimens. In comparison, the location of the maximum reduction of crosssectional area only corresponded with the fracture location (within  $\pm$ 5% of the total gauge length) in 58 out of 120 (48.0%) specimens and the location of the largest pore only corresponded with the fracture location (within  $\pm 5\%$  of the total gauge length) in 59 out of 120 (49.0%) specimens. Additionally, Erickson et al. [35] showed strong correlations (> |0.75|) between the maximum VDF value and post-yielding mechanical properties (ultimate tensile strength, elongation, and toughness modulus). Although the VDF derived by Erickson et al. [35] demonstrated significant improvement compared to previously reported pore-related metrics, the derivation made certain assumptions that limit its applicability. For example,

the original VDF does not account for non-spherical pore shapes and pore-pore interactions, which have both been shown to have significant impacts on fracture behavior in AM metals [24,36].

In the presented work, there are two main objectives. The first objective is to extend the formulation of the previously proposed VDF presented by Erickson et al. [35] to include the impact of nonspherical pores and pore-pore interactions; the new VDF will be referred to as the modified VDF herein. Using the simulated data provided by Erickson et al. [35], the fracture-location prediction capability of the modified VDF is compared to those of the original VDF and common pore-related metrics. The second objective is to experimentally evaluate and assess the modified VDF using a set of IN718 mesoscale tensile specimens manufactured by laser powder bed fusion (L-PBF), thereby extending the test cases beyond the simulated data set presented by Erickson.

#### 2. Modification of the void descriptor function

Erickson et al. [35] derived the void descriptor function (VDF) to characterize pore networks in ductile metals. It can also potentially serve as an indicator for fracture location and as a parameter to assist with predicting post-yielding mechanical properties (ultimate tensile strength, elongation at failure, and toughness modulus). The original VDF derivation by Erickson is inspired by a Laplace radial distribution function used in the work of von Lilienfeld et al. [37] and combines fraction porosity, pore position along the axial direction (clustering), and pore distance to the nearest free surface into a single metric, expressed as:

$$VDF(z_{ref}, P) = \sum_{i=1}^{n} \frac{\nu_i e^{-\frac{S_i}{at} - \frac{|c-r_i|}{\rho c}}}{V_{gauge}},$$
(1)

where  $z_{ref}$  is a given reference point along the axial direction of the specimen (assumed to be the z direction<sup>1</sup>) and P is an array of pore attributes consisting of the individual pore volume  $(v_i)$ , pore diameter  $(D_i)$ , and pore centroid  $(x_i, y_i, z_i)$  for all n pores in the specimen. The length of the gauge section is L, the total volume of the gauge region is  $V_{gauge}$ , and the maximum distance from the centroid of the specimen cross section to the free surface is c (depicted in Fig. 1b). In Eq. (1),  $S_i$  (depicted in Fig. 1a) represents the distance from the reference position,  $z_{ref}$ , to the centroid of the  $i^{th}$  pore, measured along the axial direction:

$$S_i = \left| z_i - z_{ref} \right|, \tag{2}$$

and  $r_i$  is the distance from the farthest edge of the pore to the centroid of the specimen cross section, illustrated in Fig. 1b and calculated as follows:

$$r_i = \sqrt{x_i^2 + y_i^2} + \frac{D_i}{2}. (3)$$

In Eq. (1), the term  $\frac{S_i}{\alpha L}$  accounts for pore clustering along the axial direction of the gauge section, and  $\alpha$  is a weighting parameter that controls the relative influence of a given pore based on its axial position with respect to the point of reference. The term  $\frac{|c-r_i|}{\rho c}$  accounts for pore proximity to free surfaces, where  $\rho$  is a weighting parameter that controls the relative influence of a given pore based on its position relative to the free surface of the specimen. Erickson et al. [35] performed a Bayesian optimization to find the optimal fitting parameters ( $\alpha$  and  $\rho$ ) by maximizing the correlation between the location of the VDF global maximum and the actual fracture location. They found the optimized values for  $\alpha$  and  $\rho$  to be 0.220 and 0.188, respectively. The reader is referred to Ref [35] for the complete derivation of the original VDF.

<sup>&</sup>lt;sup>1</sup> The original formulation expresses VDF as a function of  $x_{ref}$  because of the assumed alignment of the specimen longitudinal axis with the x direction.

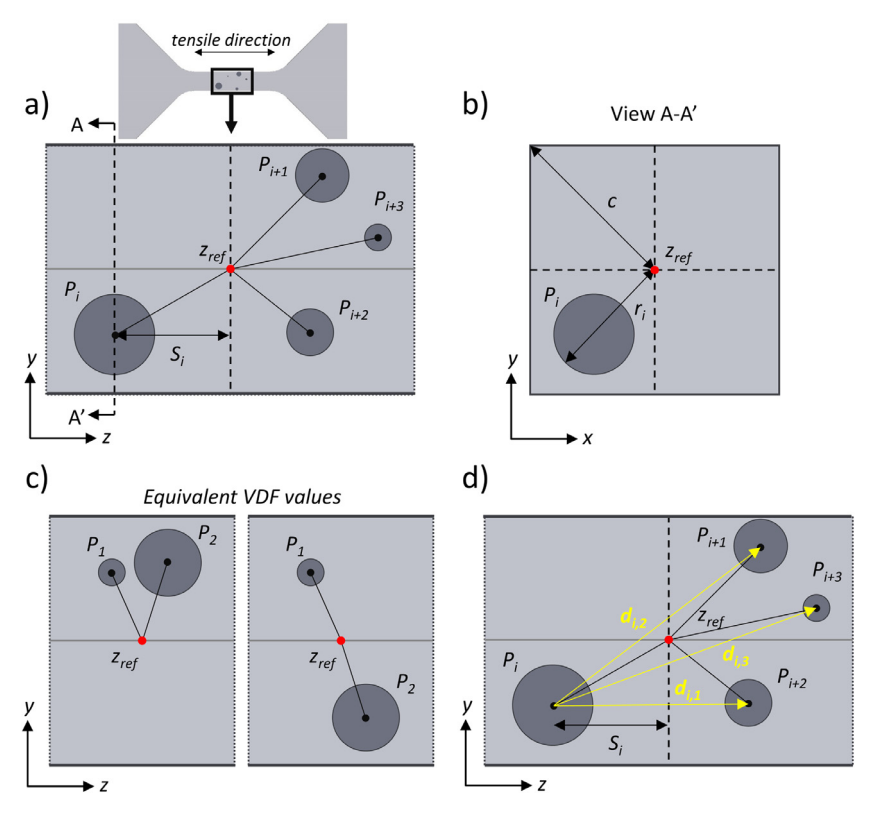


**Fig. 1.** Magnified view of specimen gauge section illustrating parameters used in the original and modified VDF formulations, where the z axis is aligned with the longitudinal axis of the tensile specimen. a) Magnified view along the gauge length, adapted from Ref. [35]. b) View of the gauge cross section, adapted from Ref. [35]. c) Limitation of the original VDF, where two instances have the same VDF value despite having different interactions between  $P_1$  and  $P_2$ . d) Proposed improvement to original VDF by incorporating pore-pore interactions using the parameter  $d_{i,j}$ .

The results from the original VDF formulation by Erickson et al. [35] were compared to failure predictions using a finite element (FE) modeling framework. Erickson et al. [35] created 120 FE models of AM 17-4 PH stainless steel uniaxial tensile specimens with statistically similar closed-pore networks (i.e., isolated, nonoverlapping pores), assuming spherical pores. The number of pores, pore sizes, and pore locations were sampled from distributions based on experimental measurements of AM 17-4PH stainless steel by Boyce et al. [38]. The pores were explicitly modeled, and an isotropic elastic-plastic constitutive model with von Mises plasticity and material hardening was applied. Failure was simulated using the element deletion method. Details of the pore modeling and simulations can be found in Erickson et al. [35]. Based on the computational fracture simulations, Erickson's VDF metric was shown to outperform common pore-related metrics reported in the literature in terms of its ability to predict fracture location and its correlation with post-yielding mechanical properties.

Despite the promising results from Erickson's original VDF work, there are two limitations in the original formulation that are addressed in this work: the lack of pore-pore interactions and the assumption that the pores are spherically shaped. First, although Erickson's VDF formulation does account for pore clustering relative to a given reference point ( $z_{ref}$ ), it does not account for pore-pore interaction. Fig. 1c illustrates this limitation by showing two scenarios that would result in equivalent values of VDF despite having obvious differences in the interactions between the two pores  $P_1$  and  $P_2$ . For Erickson's VDF formulation, the two cases have the same VDF value because the distance from  $z_{ref}$  to  $P_2$  is identical in both cases, and there is no term in Eq. (1) that accounts for the distance between  $P_1$  and  $P_2$ . Realistically, the case on the left in Fig. 1c would be considered more critical than the one on the right due to the interacting stress fields between the two pores, which

could impact the fracture behavior. Yadollahi et al. [36] showed a higher rate of pore coalescence in specimens having more closely spaced nearest-neighbor pores in AM steels than those with more distant neighbors. They attributed this increase in pore coalescence rates to the increased interactions of the pores' stress fields. The second limitation of the original VDF is the assumption that all pores are spherical. It is well documented that pores or voids in AM metals can range from spherical to highly non-spherical, depending on the mechanism of void formation [22]. Irregularly shaped (non-spherical) pores can impact more negatively the tensile behavior than spherical pores, depending on their orientation relative to the loading direction [24], and have been shown to contribute to crack initiation (e.g., see Ref. [39]). Because Erickson's original VDF formulation assumes every pore is spherical, it does not account for the range of pore morphologies that are observed in AM metals. Thus, this work seeks to extend the VDF to address both of the aforementioned limitations.

#### 2.1. Pore-pore interaction

To account for pore-pore interactions in the modified VDF formulation, a nearest-neighbor calculation is performed for each pore (as shown in Fig. 1d), and the VDF formulation is enriched with a weighted nearest-neighbor distance term,  $a_i$ , while maintaining the same Laplacian function form that was used in the original derivation. The term  $a_i$  accounts for pore-pore interactions via a weighted nearest-neighbor calculation, as follows:

$$a_i = \frac{\sum_{j=1}^{n-1} w_j d_{i,j}}{d_{i,max}},\tag{4}$$

where w is an array of length n-1 used to assign weights to all neighboring pores. In this work, a linear weighting is used such

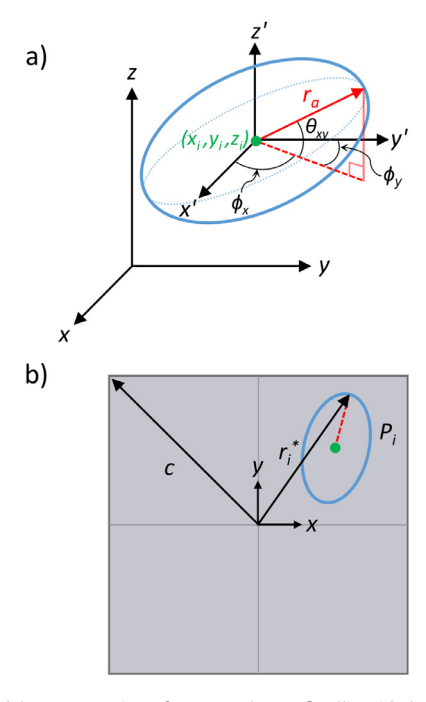


**Fig. 2.** Ellipsoidal representation of pore  $P_i$ . a) Best-fit ellipsoid showing the major semi-axis length  $(r_a)$ , the angle between vector  $\vec{r}_a$  and the projection of  $\vec{r}_a$  in the x-y plane  $(\theta_{xy})$ , the angles between the projection of  $\vec{r}_a$  and the x axis  $(\phi_x)$  and the projection of  $\vec{r}_a$  and the y axis  $(\phi_y)$ , and the centroid of the ellipsoid  $(x_i, y_i, z_i)$ . b) The projected ellipse in the x-y plane and the definitions of  $r_i^*$  and c used in the modified VDF formulation

that the array consists of evenly spaced values ranging from 1 to 0, which, for a given pore, will weight closer pores more heavily than distant pores. The array of nearest-neighbor distances, d, is arranged closest to farthest and measures the distance between the centroids of the  $i^{\rm th}$  and  $j^{\rm th}$  pores. The  $a_i$  term is normalized by dividing by the maximum value of the neighbor distances  $d_{i,max}$ .

#### 2.2. Non-spherical pores

To account for non-spherical pores, and the stress concentrations that they can induce, the pores are fitted using ellipsoids rather than spheres. Fit parameters for each ellipsoid include the major semi-axis length  $(r_a)$ , the minor semi-axes  $(r_b, r_c)$ , and the angles  $\theta_{xy}$ ,  $\phi_x$ , and  $\phi_y$  depicted in Fig. 2a. The value of  $r_i$  from the original derivation is updated to account for non-spherical pore shapes. Referring to Fig. 2, the updated value,  $r_i^*$ , is calculated as:

$$r_i^* = \sqrt{(x_i + r_a \cos(\theta_{xy}) \cos(\phi_x))^2 + (y_i + r_a \cos(\theta_{xy}) \cos(\phi_y))^2}.$$
(5)

Additionally, a stress-concentration-factor term,  $k_i$ , is added to the modified VDF that accounts for both pore ellipticity and orientation relative to the loading axis, which is expressed as:

$$k_i = \Psi_i \frac{K_{t,i}}{K_{t,max}},\tag{6}$$

where  $\Psi_i$  and  $K_{t,i}$  represent the sphericity and orientation-dependent stress concentration factor, respectively, for the  $i^{th}$  pore, and  $K_{t,max}$  is the maximum value of  $K_t$  among the population of pores in a given sample. The sphericity is calculated as follows [40]:

$$\Psi_{i} = \frac{\sqrt[3]{36\pi \, v_{i}^{2}}}{A_{i}},\tag{7}$$

where  $A_i$  is the surface area of the pore. For simplicity, and without loss of generality,  $K_t$  corresponds to the stress concentration factor for an elliptical hole in a two-dimensional infinite plate subjected to remotely applied uniaxial tension based on the theoretical stress derivation by Inglis [41]. In the most severe case, in which the major axis of the ellipse is perpendicular to the loading axis, the stress concentration factor is calculated as [42,43]:

$$K_{t}(\beta = \frac{\pi}{2}) = 1 + 2\frac{r_{a}}{r_{b}},$$
 (8)

where  $\beta$  represents the angle between the loading axis and the major axis of the elliptical hole. In the least severe case, in which the major axis of the ellipse is parallel to the loading axis, the stress concentration factor is calculated as:

$$K_t(\beta = 0) = 1 + 2\frac{r_b}{r_a}.$$
 (9)

For any arbitrary orientation,  $\beta$  (or  $\pi/2 - \theta_{xy}$ , as shown in Fig. 2a), the stress concentration factor can be approximated using a linear interpolation of  $K_t$  between the two extreme cases described above:

$$K_t(\beta) = \left(K_t(\beta = \frac{\pi}{2}) - K_t(\beta = 0)\right) \frac{\beta}{\pi/2} + K_t(\beta = 0).$$
 (10)

# 2.3. Modified VDF formulation

The final, modified VDF is expressed as:

$$VDF(z_{ref}, P) = \sum_{i=1}^{n} \frac{v_i e^{-\frac{S_i}{\alpha t} - \frac{\left|c - r_i^*\right|}{\rho c} - \frac{a_i}{\gamma} - \frac{k_i}{\zeta}}}{V_{gauge}}.$$
 (11)

The scaling parameters  $\gamma$  and  $\zeta$  control the rate of exponential decay used to express the relative influence of a given pore on the VDF value in terms of its interactions with all other pores in the specimen  $(\gamma)$  and the stress concentration associated with its shape and orientation  $(\zeta)$ . An overview of the implementation of the VDF calculation is provided in Algorithm 1, and the corresponding Python code is provided via GitHub (see Data Availability).

Prior to experimental evaluation using the mesoscale tensile specimens, the modified VDF is assessed by revisiting the computational results from Erickson et al. [35].

## 3. Materials and methods

An experimental evaluation of the modified VDF formulation was carried out using mesoscale tensile specimens machined from the grip sections of AM IN718 fatigue specimens studied previously by Watring et al. [12]. The specimens were fabricated using a 3D Systems<sup>2</sup> ProX DMP 320 machine and IN718 powder. In the previous study [12], 25 unique build conditions were investigated in terms of their impact on total fatigue life. It was found that, of three build orientations considered, the 0° and 60° build orientations resulted in the minimum and maximum fatigue lifetimes, respectively, for a given value of laser-energy density. Furthermore, for a given build orientation, the total fatigue life versus laserenergy density exhibited a bell-shaped curve, with a maximum fatigue life corresponding to a laser-energy density of approximately 62 J/mm<sup>3</sup>. Of the 25 build conditions considered previously, the two build conditions representing the best fatigue performance for the 0° and 60° build orientations are selected for the current study. Table 1 shows the L-PBF parameters used to fabricate the speci-

<sup>&</sup>lt;sup>2</sup> Certain commercial software, equipment, instruments or materials are identified in this paper to adequately specify the experimental procedure. Such identification is not intended to imply recommendation or endorsement by the National Institute of Standards and Technology, nor is it intended to imply that the equipment or materials identified are necessarily the best available for the purpose.

# Algorithm 1: Modified VDF formulation.

**For** each  $z_{ref}$  in L

For pore i from 1 to n, where n is the total number of pores

> **Step 1:** Calculate effect of pore-pore interactions,  $a_i$ For j=1 to n-1

> > Generate linearly spaced weight vector  $w_i$ from 1 to 0

> > Generate nearest-neighbor distance vector

Calculate 
$$a_i = \frac{\sum_{j=1}^{n-1} w_j d_{i,j}}{d_{i,max}}$$

Calculate  $a_i = \frac{\sum_{j=1}^{n-1} w_j d_{i,j}}{d_{i,max}}$  **Step 2:** Calculate effect of pore clustering along gauge length, Si

Calculate  $S_i = |z_i - z_{ref}|$ 

Step 3: Calculate effect of pore distance to free surface,  $|c-r_i^*|$ 

Calculate fitted ellipsoid parameters

Major semi-axis length of the ellipsoid:  $r_a$ Minor semi-axes length of the ellipsoid:  $r_h$ ,  $r_c$ Ellipsoid angles from major semi-axis:  $\theta_{xy}$ ,  $\phi_x$ , and  $\phi_y$ 

Calculate distance from centroid to edge of pore,  $r_i^*$ Calculate  $|c - r_i^*|$ 

**Step 4:** Calculate the stress concentration factor term Calculate the stress concentration factor of pore:

Calculate 
$$K_t(\beta) = \left(K_t(\beta = \frac{\pi}{2}) - K_t(\beta = 0)\right)$$

$$\frac{\beta}{\pi/2} + K_t(\beta = 0)$$
Calculate  $\Psi_i = \frac{\sqrt[3]{36\pi v_i^2}}{A_i}$ 
Calculate  $k_i = \Psi_i \frac{K_{t,i}}{K_{t,max}}$ 

**Step 5:** Calculate VDF contribution for pore *i* Sum VDF values for all pores according to Eqn. 11

Calculate VDF(
$$z_{ref}, P$$
) =  $\sum_{i=1}^{n} \frac{v_i e^{-\frac{S_i}{\alpha L} - \frac{|c-r_i^*|}{\rho c} - \frac{a_i}{\gamma} - \frac{k_i}{\zeta}}}{V_{gauge}}$ 

mens for the two build conditions. The reader is referred to previous work by Watring et al. [12,44] for more details about the

As illustrated in Fig. 3, grip regions from the previously investigated fatigue specimens [12] were sliced into thin wafers (approximately 400 µm) using wire electrical discharge machining (wire-EDM). From the wafers, mesoscale tensile specimens based on previous work from Liew et al. [45] and Benzing et al. [46] were excised (dimensions are depicted in Fig. 3d) and one surface was polished (0.05 µm final step) for microstructure characterization. The microstructure evolution will be reported in future work. Three specimens for each build condition were excised for a total of six specimens. The mesoscale tensile specimens were loaded to failure in uniaxial tension at a strain rate of 1e-3s<sup>-1</sup>, and digital image correlation via an optical microscope was used to measure engineering strain. Yield strength, ultimate tensile strength, uniform elongation, and total elongation were calculated according to practices recommended in ASTM E8-16a [47].

Prior to tensile testing, the entire gauge region of each mesoscale specimen was imaged using X-ray CT to enable 3D reconstruction and quantification of the pore structure for each specimen. A Zeiss Xradia Versa XRM500 X-ray CT machine (operated at 130kV to 160kV, 10W, and approximately 2 µm voxel edge length) was used for the X-ray CT measurements. In the CT, 1601 projection images were collected while rotating the specimen through 360°. Each projection was 1000×1000 pixels. Tomographic projections were reconstructed into a 3D volume, and then exported as TIFF image stacks using the proprietary algorithm provided in the Xradia software. Image processing, segmentation, and format conversion were conducted using a combination of custom Python scripts and FIJI [48]. DREAM.3D [49] was used to quantify the dimensions, orientation, and location of each pore (assuming a bestfit ellipsoid), which were then used to define the pore parameters in the VDF described in Section 2. Specifically, for each pore, the centroid, volume, surface area, major semi-axis length, and orientation of the major semi-axis were recorded. The fraction porosity was measured using the total volume of the pores and the total volume of the specimen observed in the CT data. The sphericity was calculated by Eq.(7). Visual reconstructions of the pore network for each specimen were performed using ParaView [50]. Following tensile testing to failure, the gauge region for each specimen was characterized again using X-ray CT. The post-fracture CT data provides a visual reconstruction of the fractured surfaces and allows for a measurement of the fracture location. Post-failure X-ray CT was conducted at a higher resolution, with voxel edge length of about 1 µm. This was achieved by using "vertical stitching" (a custom mode in the Xradia control software) to extend the vertical dimension as necessary to image the entirety of each half of the fracture gauge section. Images were then downsampled to match the resolution of the initial scans.

# 4. Results

## 4.1. X-Ray CT and porosity values

The X-ray CT measurements were used to quantify the pore structures among the mesoscale specimens. The image stack from each of the CT measurements for each specimen was converted to a Visualization Toolkit (VTK) file and visualized using ParaView [50]. The CT reconstruction is shown in Fig. 4, which illustrates both the internal pore structure and the surface topography of each specimen. Although Figs. 4a, 4b, and 4c show three different specimens from the same build condition (P1: 220W, 1180mm/s, 60° orientation), there is a slight difference in porosity: 0.04%, 0.05%, and 0.01%, respectively. This also holds true for the second build condition (P2: 330W, 1770mm/s, 0° orientation), where the first specimen (P2<sub>1</sub>) has a porosity of 0.08% compared to 0.01% and 0.02% for the second and third specimens (P22 and P23), respectively. To determine if the pore structures of specimens are significantly different, a t-test assuming unequal variances was performed between each of the specimens [51]. The results from the *t*test analysis show that for build condition P1, the mean pore sizes for the three specimens are not significantly different (p values of 0.39, 0.09, and 0.11). For build condition P2, the mean pore sizes are also not significantly different when taking p < 0.05 to be significant (p values of 0.06, 0.34, and 0.05).

Table 1 L-PBF IN718 processing parameters for the two build conditions.

Build condition	Laser power (W)	Scan speed (mm/s)	Layer thickness (µm)	Build orientation (°)	Laser-energy density (J/mm³)
P1	220	1180	30	60	62
P2	330	1770	30	0	62

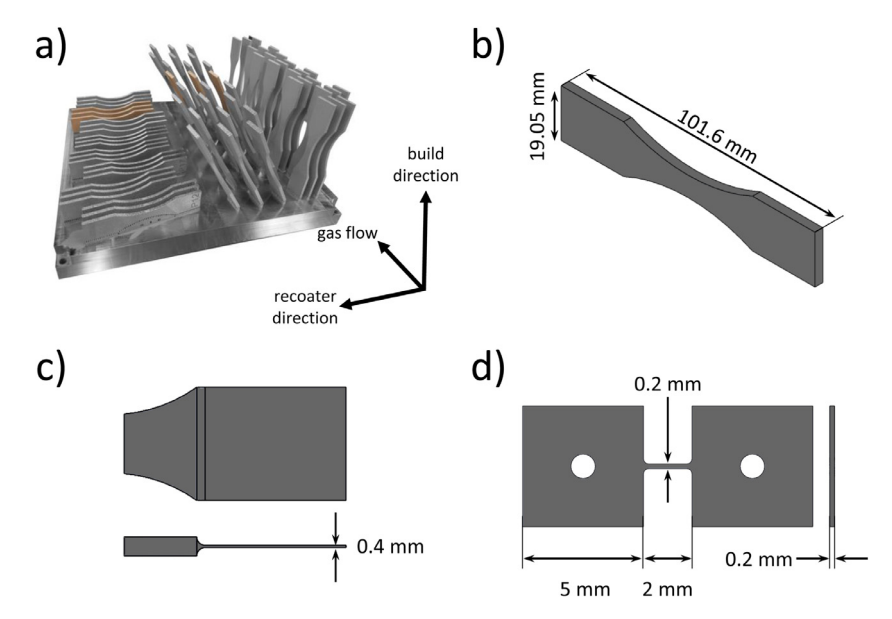


Fig. 3. Reuse of fatigue specimens from a previous study [12]. a) All as-built IN718 fatigue specimens on the build plate prior to removal; the six specimens used in the current study are highlighted (refer to electronic version for color distinction). b) Target dimensions for the fatigue specimens in accordance with ASTM E466-15. c) Thinned grip region of the fatigue specimens, from which the mesoscale specimens are excised. d) Nominal dimensions of mesoscale tensile specimens.

**Table 2**Mechanical properties for six L-PBF IN718 mesoscale specimens and bulk properties from previous work [44]. Build condition P1: 220W, 1180mm/s, 60° orientation. Build condition P2: 330W, 1770mm/s, 0° orientation.

Specimen	Yield strength (MPa)	Ultimate tensile strength (MPa)	Uniform elongation -	Total elongation -
P1 <sub>1</sub>	308	416	0.0573	0.0758
P1 <sub>2</sub>	552	668	0.0784	0.0957
P1 <sub>3</sub>	303	503	0.1070	0.1497
P1 <sub>bulk</sub> [44]	772	1070	0.2100	0.2800
P2 <sub>1</sub>	563	768	0.1174	0.1343
P2 <sub>2</sub>	541	759	0.1664	0.1868
P2 <sub>3</sub>	348	598	0.1847	0.2001
P2 <sub>bulk</sub> [44]	798	1081	0.2200	0.2900

# 4.2. Stress-strain curves and tensile properties

The stress-strain curves from the L-PBF 17-4PH simulations [35] and the mesoscale L-PBF IN718 tensile specimens are shown in Fig. 5. For the stress-strain curves from the simulations from Erickson et al. [35] (Fig. 5a), the experimental bounds for ultimate tensile strength (UTS) and elongation as measured by Boyce et al. [38] are indicated for reference. Fig. 5a demonstrates the variation in the stress-strain response for the simulated data set due to variations in the pore structures. For the mesoscale L-PBF IN718 specimens, the minimum cross-sectional area was measured by using a bounding box measurement from the CT image stack. This measurement is comparable to a caliper measurement, which was avoided due to the delicate nature of the specimens. The minimum area was used to calculate the nominal engineering stress. The mechanical properties for the six mesoscale specimens are reported in Table 2. A large amount of scatter is observed for the yield strength, ultimate tensile strength, uniform elongation, and total elongation. When comparing to the bulk properties obtained using tensile specimens with cross section of 2.54 × 1.00mm in work previously performed by the authors for the corresponding build conditions [44], the tensile properties for the mesoscale tensile specimens are significantly lower for all six specimens.

#### 4.3. Modified VDF results

Prior to the experimental evaluation performed using the mesoscale tensile specimens, an evaluation of the modified VDF formulation was performed using Erickson's numerical data [35]. The final fitting parameters based on the numerical data set are  $\alpha$ = 0.193,  $\rho$ = 0.181,  $\gamma$ = 0.698,  $\zeta$ = 1.0, which were determined using a Bayesian optimization procedure [52] similar to that performed in Ref[35]. As reported by Erickson et al. [35], the original VDF formulation was able to accurately predict (within  $\pm 5\%$  of the total gauge length) the fracture location for 91 out of 120 simulated tensile tests using the FE framework described in Section 2. For the same tolerance, the modified VDF formulation presented herein is able to predict fracture location in 94 out of 120 simulated tensile tests, representing a 3.3% increase in the number of accurately predicted fracture locations compared to the original VDF formulation. By comparing each sample within the population, it is observed that there are six FE simulations for which the modified VDF accurately predicts the fracture location and the original VDF does not (shown in Fig. 6a-f), and three simulations for which the original VDF accurately predicts the fracture location and the modified VDF does not (Fig. 6g-i), which is discussed further in Section 5.1.

The modified VDF formulation was then experimentally evaluated by comparing the fracture location in the six L-PBF IN718 mesoscale tensile specimens to the maximum VDF location. The final fitting parameters based on the experimental data set are  $\alpha$ = 0.342,  $\rho$ = 1.0,  $\gamma$ = 0.1,  $\zeta$ = 0.1, which, as before, were determined using a Bayesian optimization procedure [52] similar to that performed in Ref[35]. For comparison, both the original VDF by Erickson and the cross-sectional area reduction due to pore structures were plotted along the entire gauge length for each of the six specimens. The plots in Fig. 7 show the original and modified VDFs and the cross-sectional area reduction as a percentage. Below each plot are the X-ray CT reconstructions of the corresponding specimen in both the undeformed and fractured states, with the pores highlighted in red. For reference, the largest pore by volume in the undeformed state is circled for each specimen. Based on Erickson's original VDF, the location of the global maximum coincides with the fracture location in two out of six specimens (P13 and P21). Similarly, the location of the maximum cross-sectional area reduc-

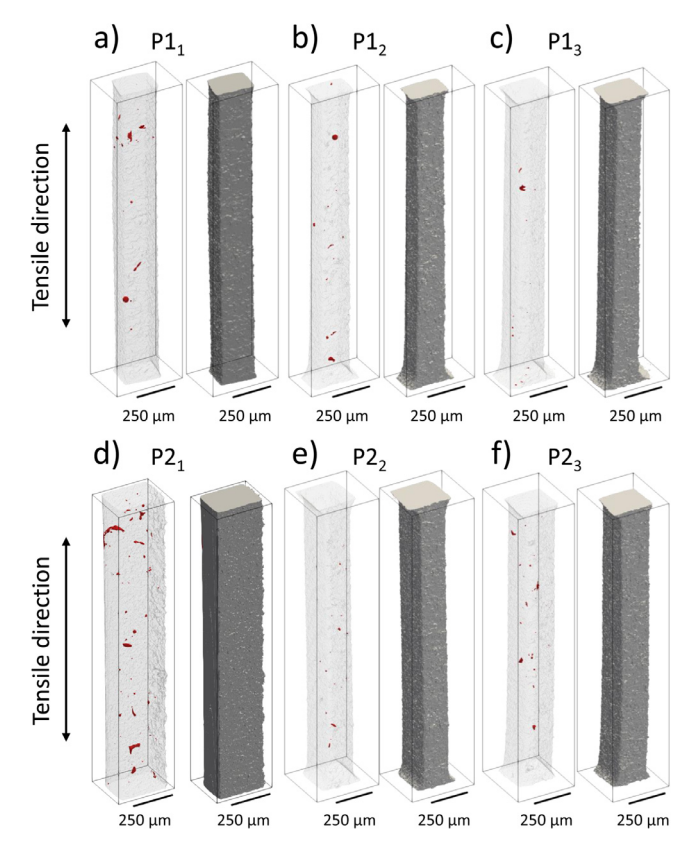


**Fig. 4.** X-ray CT reconstructions of L-PBF IN718 mesoscale specimens showing internal pore structures highlighted in red. a-c) Three specimens manufactured using build condition P1 (220W, 1180mm/s, 60° orientation). d-f) Three specimens manufactured using build condition P2 (330W, 1770mm/s, 0° orientation). Specimens were excised from larger samples using precision wire-EDM on all surfaces and one surface was finely polished for microstructure characterization (not reported in this work). (For interpretation of the references to colour in this figure legend, the reader is referred to the web version of this article.)

tion as well as that of the largest pore coincide with the fracture location in the same two specimens. On the other hand, for the modified VDF presented in this work, the location of the global maximum coincides with the fracture location in five out of the six specimens.

#### 5. Discussion

5.1. Application of the modified VDF to computational fracture simulations: Impact of pore-pore interactions

The performance of the modified VDF is first discussed in the context of the simulated fracture results investigated by Erickson et al. [35]. Recall that the simulated data set was generated using statistically representative pore size distributions extracted from experimental measurements. However, the synthetic network of simulated pores assumed a spherical shape for each pore. Because the simulated data set contains pore networks with only spherical pores, any improvement in the modified VDF on the simulated data set is attributed to pore-pore interactions (modeled by the weighted nearest-neighbor term,  $a_i$ , in Eq.(4)). Thus, the 3.3% increase in the number of accurately predicted fracture locations (94 accurate predictions using the modified VDF versus 91 using the original VDF) is due solely to accounting for pore-pore interactions.

Fig. 8a shows one of the six simulations for which the modified VDF accurately predicts the fracture location and the original VDF does not. Erickson's original VDF predicts that fracture will occur at a large pore at the beginning (left-most end) of the gauge length, labeled "1" in Fig. 8a. On the other hand, the modified VDF predicts that fracture will occur at the location labeled "2" in Fig. 8a. A pore located at point "2" in Fig. 8a is actually slightly larger than that at point "1" (equivalent spherical diameter (ESD) of 99.75 µm compared to an ESD of 96.59 µm). However, Erickson's original VDF predicts that fracture will occur at the first pore due in part to its location relative to the free surface. Although the original VDF does account for clustering of the pores with respect to a reference point along the gauge length, it does not account for pore-pore interactions. The incorporation of the weighted nearest-neighbors term into the modified VDF represents this mechanism of porepore interaction. Specifically, in Fig. 8a, the location at which the modified VDF predicts fracture to occur consists of the large pore closely surrounded by a large number of smaller pores. This observation indicates that for the simulation depicted in Fig. 8a, the weighting of pore-pore interactions relative to that of the pore size and location relative to the free surface enables accurate prediction of the fracture location. The same observation holds true for all six simulations depicted in Figs. 6a-f.

There are three cases for which the modified VDF incorrectly predicts the fracture location while the original VDF accurately

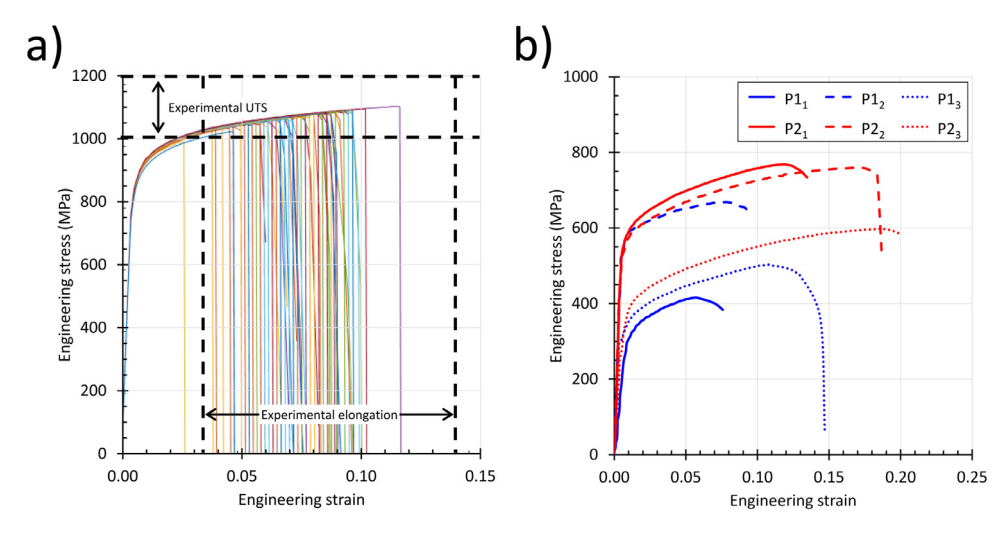


Fig. 5. Engineering stress-strain curves for a) the simulated tensile tests of L-PBF 17-4PH stainless steel from Erickson et al. [35] (experimental bounds from Ref. [38]. are included for reference) showing the variability of the mechanical response due to variations in the pore structures, and b) the six L-PBF IN718 mesoscale specimens (three repeats for two different build conditions).

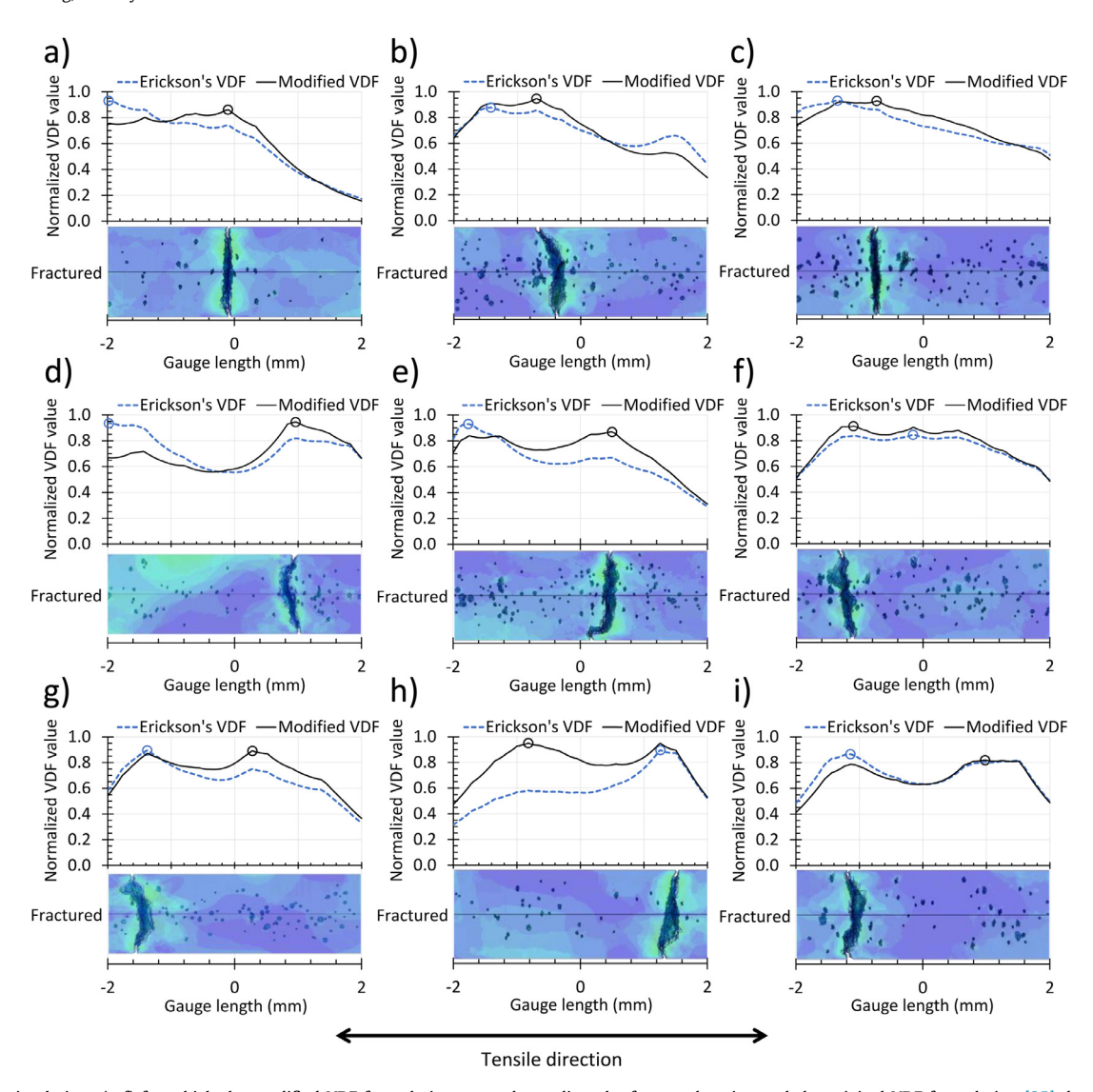


Fig. 6. The six simulations (a-f) for which the modified VDF formulation correctly predicts the fracture location and the original VDF formulation [35] does not. The three simulations (g-i) for which the original VDF formulation [35] correctly predicts the fracture location and the modified VDF formulation does not. The predicted fracture location based on maximum VDF value is circled in each case. The simulated fracture specimens from Ref[35] are presented below the plots to provide a visual comparison between VDF values, fracture location, and internal pore structures. Color contour shows von Mises stress fields overlaid to highlight locations of final fracture (taken after fracture for visualization purposes only, so stress legends are intentionally excluded).

predicts the fracture location, one of which is shown in Fig. 8b. In this example, based on Erickson's original VDF, fracture is predicted to occur at point "4", where there are two large pores (ESDs of 79.36  $\mu m$  and 90.57  $\mu m$ ) that are both located relatively close to the surface. The modified VDF predicts that fracture will occur at point "3", where there is one large pore (81.49  $\mu m$ ) surrounded by multiple small pores. In this instance, the modified VDF weights the pore-pore interaction too heavily compared to the size and the location of the pores relative to the free surface. This is similar for the three cases depicted in Fig. 6g-i, where the modified VDF incorrectly predicts the fracture location. However, the six cases for which the modified VDF outperforms the original VDF in terms of fracture-location prediction by accounting for pore-pore interaction is deemed a meaningful improvement.

The maximum value of the modified VDF ( $VDF_{max}$ ) was then compared to seven different pore-related metrics in terms of its correlation with mechanical properties, viz., elastic modulus (E), yield strength ( $\sigma_{yield}$ ), ultimate tensile strength ( $\sigma_{U}$ ), percent elongation ( $e_f$ ), and toughness modulus ( $U_f$ ). The seven pore-related metrics include fraction porosity ( $V_{frac}$ ), total number of pores ( $N_{tot}$ ), average cross-sectional area reduction ( $CSA_{ave}$ ), maxi-

mum cross-sectional area reduction ( $CSA_{max}$ ), average first nearest-neighbor distance ( $NND_{ave}$ ) across all pores, average equivalent spherical diameter ( $ESD_{ave}$ ), and maximum equivalent spherical diameter ( $ESD_{max}$ ). A Pearson correlation analysis was performed on the simulated data set. Fig. 9(a) shows the correlation values between the mechanical properties of the simulated tensile tests and the pore metrics, including the  $VDF_{max}$ . Of all metrics considered, fraction porosity, total number of pores, and average cross-sectional area reduction have the highest correlation with both the elastic modulus and the yield strength. However,  $VDF_{max}$  has the highest correlation coefficients with the post-yielding mechanical properties (i.e.,  $\sigma_U$ ,  $e_f$ ,  $U_f$ ), indicating that the modified VDF could better assist with predicting fracture-related properties than commonly reported pore metrics.

A Pearson correlation analysis was also performed between the fracture location ( $z_{fract}$ ) and the locations of  $CSA_{max}$ ,  $ESD_{max}$ , and  $VDF_{max}$ . As shown in Fig. 9b, the actual fracture location is most highly correlated with the location of  $VDF_{max}$  than with the locations of the maximum cross-sectional area reduction and the location of the largest pore. This is consistent with the results of the correlation analysis performed by Erickson et al. [35]. Erick-

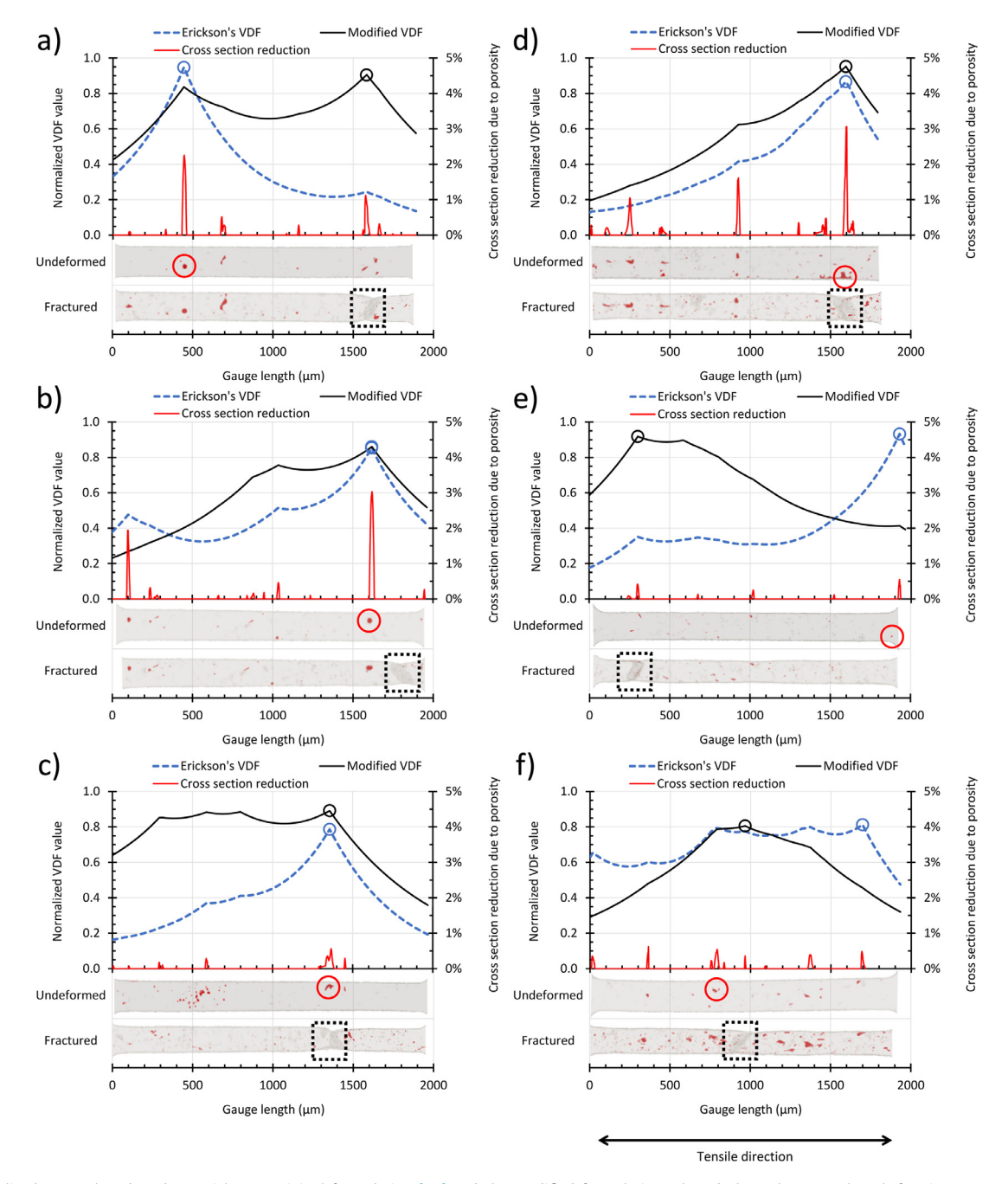


**Fig. 7.** Normalized VDF values based on Erickson's original formulation [35] and the modified formulation, plotted along the gauge length for six L-PBF IN718 mesoscale specimens machined from two different build conditions: P1 (220W, 1180mm/s, 60° orientation) and P2 (330W, 1770mm/s, 0° orientation). a) P1<sub>1</sub>, b) P1<sub>2</sub>, c) P1<sub>3</sub>, d) P2<sub>1</sub>, e) P2<sub>2</sub>, f) P2<sub>3</sub>. The predicted fracture location based on maximum VDF value is circled for each case. For each specimen, the cross-sectional area reduction due to porosity is plotted along the gauge length, and the location of the largest pore by volume is circled in red. X-ray CT reconstructions showing both the undeformed and fractured states are presented below each plot, with pores highlighted in red. (For interpretation of the references to colour in this figure legend, the reader is referred to the web version of this article.)

son et al. [35] also defined an ambiguity score to quantify the difference between global and local maxima in the VDF. A high ambiguity score indicates that the highest local maximum is similar in value to the value of the global maximum, which makes the prediction of fracture location somewhat ambiguous. They showed that applying a threshold ambiguity score of 0.7 resulted in a 97% accuracy (38 out of 39 specimens) in predicting fracture location based on the global VDF value. By applying the same ambiguity calculations and threshold of 0.7 to the modified VDF results, 34 specimens are retained, of which 30 (88.2%) have fracture locations that are accurately predicted by the location of the global

 $VDF_{\rm max}$ . The correlation coefficient between the fracture locations predicted by the  $VDF_{\rm max}$  and the actual fracture locations increases to 0.906 after applying the ambiguity threshold (Fig. 9b), which is substantially higher than the correlation coefficients corresponding to  $ESD_{\rm max}$  and  $CSA_{\rm max}$ . A visualization of this improvement can be seen in Fig. 9c, where the actual versus the predicted fracture locations based on the maximum cross-sectional area reduction, maximum pore size, maximum VDF value, and maximum VDF value for specimens with less than 0.7 ambiguity score are plotted. It is clear that by removing the more ambiguous specimens, some of the outliers (in Fig. 9c) are removed. However, some specimens that were

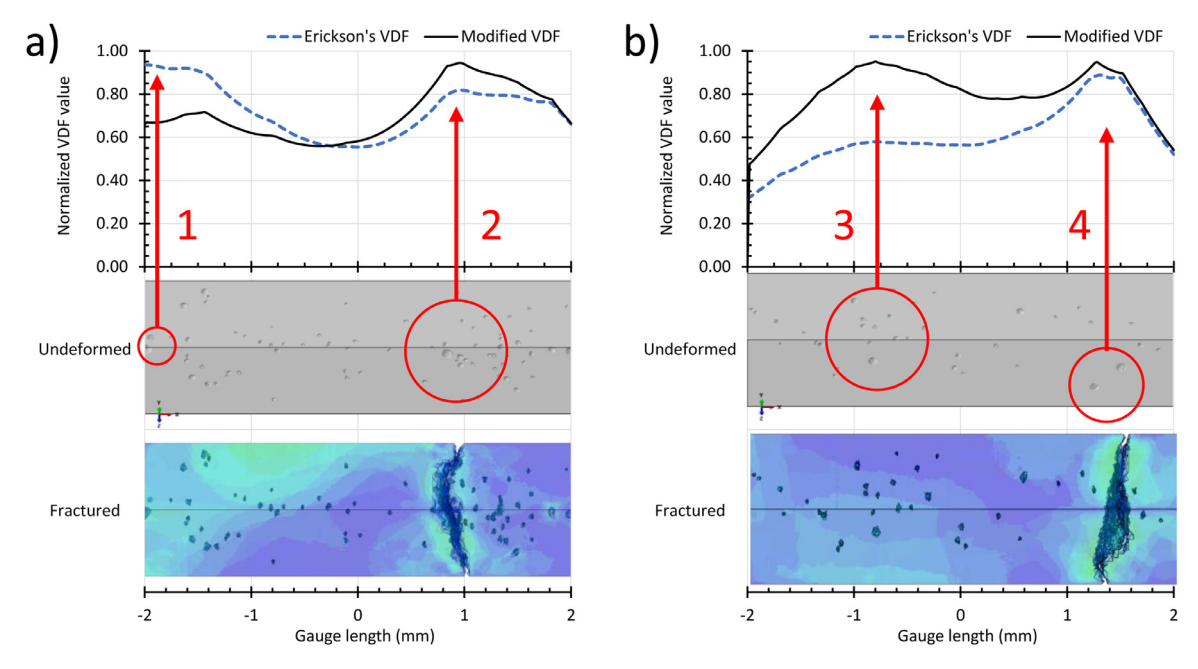
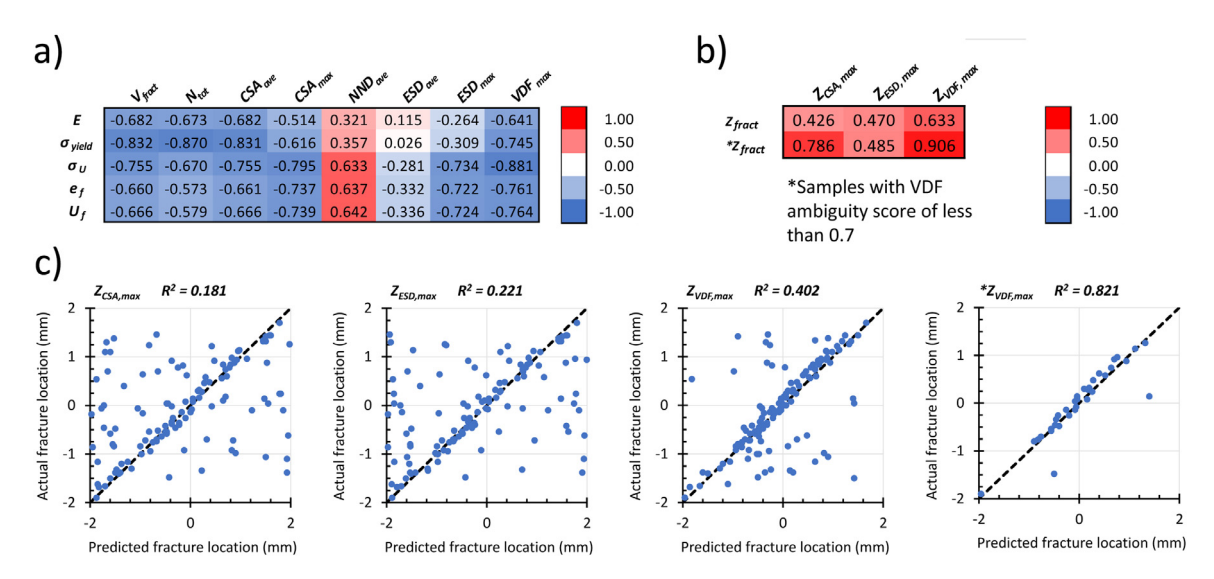


Fig. 8. Important features in the computational fracture simulations for a) a representative simulation for which the modified VDF accurately predicted the fracture location and the Erickson VDF did not, and b) a simulation for which the Erickson VDF accurately predicted fracture location and the modified VDF did not. Color contours are the same as in Fig. 6.



**Fig. 9.** a) Pearson correlation coefficients between pore metrics and mechanical properties. b) Pearson correlation coefficients between the actual fracture location and the predicted fracture locations for the maximum cross-sectional area reduction, the maximum equivalent spherical diameter, and the maximum value of the modified VDF. c) Scatter plots showing the correlation between the actual fracture locations and the predicted fracture locations.

accurately predicted with the modified VDF were removed during ambiguity thresholding, indicating that although the modified VDF generally performs better than the original VDF, the ambiguity is increased by adding the pore-pore interaction. Fig. 6e shows a clear example of this; when the pore-pore interaction is included in the VDF formulation, the VDF value for the region containing a large number of pores (around 0.4mm) increases. The modified VDF accurately predicts the fracture to occur at this location while the Erickson VDF does not, but it also increases the ambiguity of the prediction, causing it to be removed when applying an ambiguity score threshold.

In summary, the modified VDF shows a slight but meaningful improvement in fracture-location predictions compared to the Erickson VDF for the simulated fracture results. In comparison to

other pore-related metrics used to predict fracture location, the modified VDF performs exceptionally well. Recall the location of the maximum cross-sectional area reduction and the location of the largest pore accurately predicted 58 out of the 120 specimens (48%) and 59 out of the 120 specimens (49%), respectively. The modified VDF accurately predicted fracture location in 62.1% more specimens than the location of the maximum cross-sectional area reduction and 59.3% more specimens than the location of the largest pore. This shows significant improvement over the commonly used pore metrics to predict fracture location and, based on the correlation analysis with mechanical properties, suggests that the VDF is a promising metric to assist with predicting fracture-related properties in AM metals.

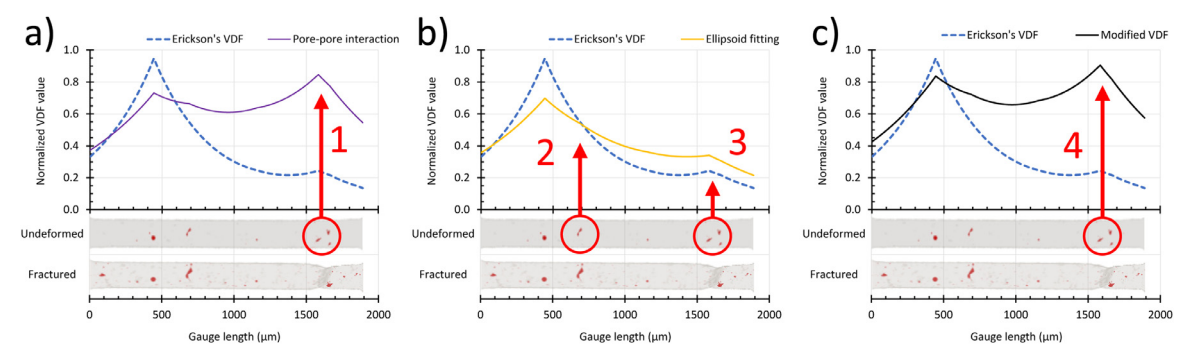


Fig. 10. Important features in one mesoscale specimen that influence the VDF formulation for a) the pore-pore interaction, b) the ellipsoid fitting, and c) the final, modified VDF formulation

# 5.2. Application of the modified VDF to experimental data: Impact of pore-pore interactions and stress concentration factors

The modified VDF is now assessed in the context of the six L-PBF IN718 mesoscale tensile specimens. The X-ray CT reconstructions in Fig. 4 show that each of the specimens contains irregularly shaped pores; whereas, the simulated data set from Erickson et al. [35] consisted only of spherical pores, making it impossible to assess the impact of accounting for ellipsoidal pores and their relative stress concentrations in the modified VDF. To decouple the impact of the pore-pore interactions and the stress concentration factor due to ellipsoid fittings for the mesoscale specimens, the modified VDF was split into VDFs containing the original terms plus either the pore-pore interaction term or the stress concentration factor term and was re-evaluated against the six mesoscale specimens. The VDF including just the pore-pore interaction term accurately predicts the fracture location for two out of the six specimens (33.3%). When looking at the maximum value of the partially modified VDF containing the stress concentration factor term, the location of the maximum value coincides with fracture location in two of the six specimens (33.3%), which are a different two specimens than those that are accurately predicted by Erickson's original VDF. The Erickson VDF also accurately predicts two of the six specimens (33.3%), which shows that, individually, the addition of each term alone does not outperform the Erickson VDF. However, once the impacts from the pore-pore interaction and the stress concentration factor are combined into the final modified VDF, the location of the maximum value accurately predicts the fracture location in five of the six specimens (83.3%).

The above observations are explored visually in Fig. 10. Fig. 10a shows the Erickson VDF plotted against the partially modified VDF containing the pore-pore interaction term. There is a clear indication at the first highlighted location that this clustering of pores greatly increases the VDF value due to the pore-pore interaction. Fig. 10b shows the impact of the stress concentration term (without pore-pore interaction). In the first highlighted section of Fig. 10b, there is an irregularly shaped pore that is relatively small in size. In the Erickson VDF, this pore does not increase the VDF value due to its small size. However, in the partially modified VDF that includes the stress concentration term, a small increase in VDF value appears at this pore's location. This shows that the modified VDF value increases at locations containing more irregularly shaped pores oriented such that stress concentration values are higher, which reflects research showing that such non-spherical pores increase localized stress concentrations and hence influence fracture behavior. The next highlighted section in Fig. 10b shows the region discussed in Fig. 10a. The observed clustering of pores has one pore that is larger than the nearby pores and is irregularly shaped. The irregular shape of this pore increases the VDF value at its corresponding location. The highlighted section in Fig. 10c shows the combined effect of the porepore interaction and the stress concentration terms. In this highlighted section, the non-spherical pore shape in conjunction with pore-pore interaction drives the VDF value to exhibit a global maximum, which correctly predicts the fracture location. This example demonstrates how each additional parameter in the modified VDF influences the VDF values.

Similar to the numerical investigation, the modified VDF was compared to the location of the maximum reduction in cross-sectional area and the location of the largest pore for the experimental data set. The location of the maximum pore size and the location of the maximum cross-sectional area reduction accurately predicted fracture location in two out of the six specimens (which were the same as those accurately predicted by the Erickson VDF), as compared to the five fracture locations accurately predicted by the modified VDF. There are no cases for which any of the other metrics correctly predict fracture location and the modified VDF does not.

There is only one specimen for which none of the metrics considered (including the modified VDF) accurately predicts the fracture location: P1<sub>2</sub>. Examining closely the CT data for P1<sub>2</sub> (Figs. 7b and 4 b), there are no obvious features in the region where fracture occurred that would indicate that fracture was driven by pores or surface roughness. This assertion was corroborated by images of the fracture surface that were recorded using a scanning electron microscope. Thus, it is postulated that fracture could have been driven by features in the grain or sub-grain structures. However, further investigation (e.g., with a crystal plasticity model that incorporates microstructure measurements made prior to tensile deformation), is required to confirm this. In summary, although the original Erickson VDF does not outperform the common pore metrics for predicting fracture in the experimental tensile specimens, the predictive capability of the VDF is improved significantly by accounting for pore-pore interactions and stress concentrations associated with pore ellipticity (the degree of deviation from sphericity) and orientations.

#### 5.3. Limitations and future work

Although this work shows significant improvement in the predictive capabilities of the VDF, there are still limitations that should be mentioned. This work focused on improving the predictive capabilities of the VDF by accounting for pore-pore interactions and stress concentrations associated with pore shape and orientation. Similar to the limitations addressed in Erickson et al. [35], this work neglects the effects of surface roughness. However, surface roughness is known to play a critical role in the mechanical response of AM metals, especially fatigue life [12,53–56]. The mesoscale specimens presented in this work were excised via wire-EDM, which removed the as-built surface roughness imparted

by the L-PBF process. However, there could still be local surface roughness features from the EDM re-cast layer that might have affected the tensile properties. For applications in which the asbuilt surface remains intact, the surface roughness would depend on geometry, processing parameters, and build orientation, which could have a significant impact on the mechanical behavior. Another current limitation of the modified VDF formulation is that both the Erickson VDF and the modified VDF presented in this work assume a one-dimensional problem using uniaxial tensile testing (i.e., VDF is expressed as a function of position along the loading axis). Additionally, AM metals have been shown to exhibit anisotropic mechanical behavior with respect to build orientation [57]. The elliptical-pore equation considers a stress raiser in the 2D xy-plane; this simplification permits the use of well-known analytical solutions for the stress concentration factors for planes in uniaxial tension. In practice, however, pores are three-dimensional and could be arranged such that the 2D plane does not capture the maximal stress concentration caused. We chose to avoid capturing arbitrarily oriented and shaped 3D ellipsoids because the analytical descriptions of their stress fields are overly complex for the perceived benefit that they would provide. Although it would be possible to include analytical or empirical forms that describe the 3D stress fields more accurately if needed, the added complexity of such an approach would undermine the stated goal of the VDF as a simple predictive tool, and furthermore, 3D formulations of the stress concentrations were not needed to improve the accuracy of the modified VDF for the present circumstances. In summary, future work could focus on extending the VDF formulation to account for surface roughness, multi-axial loading, anisotropic behavior, and more complex, three-dimensional fracture morphologies.

Although there are still limitations pertaining to the general application of the VDF to complex AM parts, the modified VDF shows significant improvement over common pore metrics in predicting the fracture location and correlating with fracture-related mechanical properties. The VDF improves upon pore-related metrics commonly reported in the literature by simultaneously accounting for pore sizes, pore shapes, pore orientations, pore clustering, pore-pore interaction, and pore locations relative to free surfaces of the specimen.

#### 6. Conclusion

In this study, the void descriptor function (VDF) derived by Erickson et al. [35] was modified by incorporating terms to account for pore-pore interactions and the stress concentrations associated with pore shapes (as measured by ellipticity) and orientations. The simulated data set from Erickson et al. [35], in which uniaxial tensile testing was simulated in AM 17-4PH stainless steel containing explicitly represented pore structures was first used to compare the modified VDF to Erickson's original VDF and to other common pore-related metrics. After analyzing the modified VDF using the simulated data set, six mesoscale IN718 specimens manufactured by laser powder bed fusion were used to experimentally evaluate the modified VDF. Based on the results from the application of the modified VDF to both the simulated data set and the experimental measurements using the mesoscale tensile specimens, the following conclusions are made:

1. The incorporation of the pore-pore interaction term using weighted nearest neighbors resulted in accurate fracture-location predictions (within  $\pm 5\%$  of the total gauge length) for 94 out of 120 specimens from the simulated data set, an increase of 3.3% compared to the number of accurate predictions based on Erickson's original VDF. Although the modified VDF showed only a slight improvement compared to the Erickson VDF, the VDF in general shows significant improvement over

- commonly reported pore-related metrics. Remarkably, the modified VDF accurately predicted fracture location in 62.1% more specimens than predicted based on the location of the maximum cross-sectional area reduction and 59.3% more specimens than predictions based on the location of the largest pore.
- 2. The improvement of the modified VDF due to the ellipsoid fitting is more complex to quantify. However, the modified VDF, combining both the pore-pore interaction and the stress concentration factor associated with pore ellipticity, accurately predicted fracture location in five out of six specimens in the experimental evaluation compared to only two out of six specimens for the original VDF, the maximum reduction in crosssectional area, and the location of the largest pore by volume. This is the first time the VDF has been experimentally evaluated, and it shows improved predictive capability for fracture location in experimental specimens over pore metrics commonly reported in the literature. To maintain accurate predictions of pore-driven fracture location for different pore populations, simple recalibration of the VDF fitting parameters is the only necessary step since the model is derived using dimensionless quantities.
- 3. Based on the simulated data set, the maximum value of the modified VDF shows a stronger correlation with post-yielding mechanical properties (ultimate tensile strength, elongation, and toughness modulus) than any of the following pore metrics: fraction porosity, total number of pores, maximum pore size, average pore size, and maximum cross-sectional area reduction. This indicates that the VDF is a promising metric to assist with characterizing pore networks and predicting ductilemetal failure properties, including for AM metals.
- 4. The promising results from the assessment of the modified VDF against both the simulated data set and the experimental, mesoscale tensile specimens demonstrate that pore-pore interaction, pore shape, and orientation with respect to loading direction play important roles in the fracture behavior of porous AM metals. The development of metrics that account for interactions among different mechanisms driving failure in AM metals is vital for the incorporation of AM metals into fracture-critical applications.

#### 7. Data availability

The source code used to calculate the VDF can be found at: https://www.github.com/mmmutah/mVDF.

# **Declaration of Competing Interest**

The authors declare that they have no known competing financial interests or personal relationships that could have appeared to influence the work reported in this paper.

# Acknowledgements

This research is supported by the Department of Defense Office of Economic Adjustment (ST1605-19-03) and by the National Science Foundation CAREER award (CMMI 1752400). The authors would like to express gratitude to 3D Systems for supplying the materials. This research was performed while Jake Benzing, Orion Kafka, and Newell Moser held National Research Council Postdoctoral Research Associateships at the National Institute of Standards and Technology.

# References

[1] J.-P. Kruth, M.-C. Leu, T. Nakagawa, Progress in additive manufacturing and rapid prototyping, CIRP Ann. 47 (2) (1998) 525–540.

- [2] M. Rehnberg, S. Ponte, 3D printing and global value chains: how a new technology may restructure global production, Global Production Networks Centre: Singapore, Copenhagen Business, School (2016).
- [3] Y. Huang, M.C. Leu, J. Mazumder, A. Donmez, Additive manufacturing: current state, future potential, gaps and needs, and recommendations, J. Manuf. Sci. Eng. 137 (1) (2015).
- [4] M. Baumers, Economic aspects of additive manufacturing: benefits, costs and energy consumption, Loughborough Universitys, 2012 Ph.D. thesis.
- [5] J.J. Lewandowski, M. Seifi, Metal additive manufacturing: a review of mechanical properties, Annu Rev Mater Res 46 (2016) 151–186.
  [6] P. Wang, M.L.S. Nai, X. Tan, W.J. Sin, S.B. Tor, J. Wei, Anisotropic mechanical
- [6] P. Wang, M.L.S. Nai, X. Tan, W.J. Sin, S.B. Tor, J. Wei, Anisotropic mechanical properties in a big-sized Ti-6Al-4V plate fabricated by electron beam melting, in: TMS 2016 145th Annual Meeting & Exhibition, Springer, 2016, pp. 5–12.
- [7] P. Wang, X. Tan, M.L.S. Nai, S.B. Tor, J. Wei, Spatial and geometrical-based characterization of microstructure and microhardness for an electron beam melted ti-6Al-4V component, Materials & Design 95 (2016) 287–295.
- [8] X.P. Tan, P. Wang, Y. Kok, W.Q. Toh, Z. Sun, S. Nai, M. Descoins, D. Mangelinck, E. Liu, S.B. Tor, Carbide precipitation characteristics in additive manufacturing of Co-Cr-Mo alloy via selective electron beam melting, Scr Mater 143 (2018) 117–121
- [9] S.S. Al-Bermani, M.L. Blackmore, W. Zhang, I. Todd, The origin of microstructural diversity, texture, and mechanical properties in electron beam melted ti-6Al-4V, Metallurgical and Materials Transactions A 41 (13) (2010) 3422–3434.
- [10] B. Song, X. Zhao, S. Li, C. Han, Q. Wei, S. Wen, J. Liu, Y. Shi, Differences in microstructure and properties between selective laser melting and traditional manufacturing for fabrication of metal parts: a review, Frontiers of Mechanical Engineering 10 (2) (2015) 111–125.
- [11] W.E. Frazier, Metal additive manufacturing: a review, J Mater Eng Perform 23 (6) (2014) 1917–1928.
- [12] D.S. Watring, K.C. Carter, D. Crouse, B. Raeymaekers, A.D. Spear, Mechanisms driving high-cycle fatigue life of as-built inconel 718 processed by laser powder bed fusion, Materials Science and Engineering: A 761 (2019) 137993, doi:10.1016/j.msea.2019.06.003.
- [13] M. Salarian, H. Asgari, M. Vlasea, Pore space characteristics and corresponding effect on tensile properties of inconel 625 fabricated via laser powder bed fusion, Materials Science and Engineering: A 769 (2020) 138525.
- [14] R. Snell, S. Tammas-Williams, L. Chechik, A. Lyle, E. Hernández-Nava, C. Boig, G. Panoutsos, I. Todd, Methods for rapid pore classification in metal additive manufacturing, JOM (2019) 1–9.
- [15] M. Tang, P.C. Pistorius, J.L. Beuth, Prediction of lack-of-fusion porosity for powder bed fusion, Addit. Manuf. 14 (2017) 39–48.
- [16] G. Vastola, Q.X. Pei, Y.-W. Zhang, Predictive model for porosity in powder-bed fusion additive manufacturing at high beam energy regime, Addit. Manuf. 22 (2018) 817–822.
- [17] C. Kamath, B. El-Dasher, G.F. Gallegos, W.E. King, A. Sisto, Density of additive-ly-manufactured, 316L SS parts using laser powder-bed fusion at powers up to 400 w, The International Journal of Advanced Manufacturing Technology 74 (1) (2014) 65–78.
- [18] N. Kouraytem, X. Li, R. Cunningham, C. Zhao, N. Parab, T. Sun, A.D. Rollett, A.D. Spear, W. Tan, Effect of laser-matter interaction on molten pool flow and keyhole dynamics, Phys Rev Appl 11 (6) (2019) 064054.
- [19] L. Sheridan, O.E. Scott-Emuakpor, T. George, J.E. Gockel, Relating porosity to fatigue failure in additively manufactured alloy 718, Materials Science and Engineering: A 727 (2018) 170–176.
- [20] E. Lucon, J. Benzing, N. Hrabe, Effect of precrack configuration and lack-of-fusion on the elastic-plastic fracture toughness of additively manufactured ti-6Al-4V parts, Mater. Perform. Charact. 9 (5) (2020).
- [21] E. Lucon, J. Benzing, N. Derimow, N. Hrabe, Small Punch Testing to Estimate the Tensile and Fracture Properties of Additively Manufactured Ti-6Al-4V, Journal of Materials Engineering and Performance (2021), doi:10.1007/s11665-021-05603-9.
- [22] A. Sola, A. Nouri, Microstructural porosity in additive manufacturing: the formation and detection of pores in metal parts fabricated by powder bed fusion, Journal of Advanced Manufacturing and Processing 1 (3) (2019) e10021.
- [23] D. Dai, D. Gu, H. Zhang, J. Xiong, C. Ma, C. Hong, R. Poprawe, Influence of scan strategy and molten pool configuration on microstructures and tensile properties of selective laser melting additive manufactured aluminum based parts, Optics & Laser Technology 99 (2018) 91–100.
- [24] A. Hilaire, E. Andrieu, X. Wu, High-temperature mechanical properties of alloy 718 produced by laser powder bed fusion with different processing parameters, Addit. Manuf. 26 (2019) 147–160.
- [25] V. Tvergaard, Material failure by void growth to coalescence, Advances in Applied Mechanics 27 (1989) 83–151.
- [26] A.L. Gurson, Continuum theory of ductile rupture by void nucleation and growth: Part I Yield criteria and flow rules for porous ductile media, (1977).
- [27] T.-S. Cao, M. Mazière, K. Danas, J. Besson, A model for ductile damage prediction at low stress triaxialities incorporating void shape change and void rotation, Int J Solids Struct 63 (2015) 240–263.
- [28] F. Fritzen, S. Forest, T. Böhlke, D. Kondo, T. Kanit, Computational homogenization of elasto-plastic porous metals, Int. J. Plast. 29 (2012) 102–119.
- [29] Y.-K. Khdir, T. Kanit, F. Zaïri, M. Naït-Abdelaziz, A computational homogenization of random porous media: effect of void shape and void content on the overall yield surface, European Journal of Mechanics-A/Solids 49 (2015) 137–145.

- [30] V. Tvergaard, Influence of voids on shear band instabilities under plane strain conditions, Int. J. Fract. 17 (4) (1981) 389–407.
- [31] O.L. Kafka, K.K. Jones, C. Yu, P. Cheng, W.K. Liu, Image-based multiscale modeling with spatially varying microstructures from experiments: demonstration with additively manufactured metal in fatigue and fracture, J Mech Phys Solids (2021) 104350, doi:10.1016/j.jmps.2021.104350.
- [32] G. Antou, G. Montavon, F. Hlawka, A. Cornet, C. Coddet, Characterizations of the pore-crack network architecture of thermal-sprayed coatings, Mater Charact 53 (5) (2004) 361–372.
- [33] A. Du Plessis, I. Yadroitsava, S.G. Le Roux, I. Yadroitsev, J. Fieres, C. Reinhart, P. Rossouw, Prediction of mechanical performance of Ti6Al4Vcast alloy based on microCT-based load simulation, J Alloys Compd 724 (2017) 267–274.
- [34] J.D. Madison, O.D. Underwood, L.P. Swiler, B.L. Boyce, B.H. Jared, J.M. Rodelas, B.C. Salzbrenner, Corroborating tomographic defect metrics with mechanical response in an additively manufactured precipitation-hardened stainless steel, in: AIP Conference Proceedings, volume 1949, AIP Publishing LLC, 2018, p. 020009.
- [35] J.M. Erickson, A. Rahman, A.D. Spear, A void descriptor function to uniquely characterize pore networks and predict ductile-metal failure properties, Int. J. Fract. 225 (1) (2020) 47–67.
- [36] A. Yadollahi, N. Shamsaei, Y. Hammi, M.F. Horstemeyer, Quantification of tensile damage evolution in additive manufactured austenitic stainless steels, Materials Science and Engineering: A 657 (2016) 399–405.
- [37] O.A. Von Lilienfeld, R. Ramakrishnan, M. Rupp, A. Knoll, Fourier series of atomic radial distribution functions: a molecular fingerprint for machine learning models of quantum chemical properties, Int J Quantum Chem 115 (16) (2015) 1084–1093.
- [38] B.L. Boyce, B.C. Salzbrenner, J.M. Rodelas, L.P. Swiler, J.D. Madison, B.H. Jared, Y.-L. Shen, Extreme-value statistics reveal rare failure-critical defects in additive manufacturing, Adv Eng Mater 19 (8) (2017) 1700102.
- [39] Z. Li, Y. Jing, H. Guo, X. Sun, K. Yu, A. Yu, X. Jiang, X.J. Yang, Study of 3D pores and its relationship with crack initiation factors of aluminum alloy die castings, Metallurgical and Materials Transactions B 50 (3) (2019) 1204–1212.
- [40] H. Wadell, Volume, shape, and roundness of quartz particles, J. Geol. 43 (3) (1935) 250–280.
- [41] C.E. Inglis, Stresses in a plate due to the presence of cracks and sharp corners, Trans Inst Naval Archit 55 (1913) 219–241.
- [42] W.D. Pilkey, D.F. Pilkey, Z. Bi, Peterson's stress concentration factors, John Wiley & Sons, 2020.
- [43] W.D. Pilkey, Formulas for stress, Strain and Structural Matrices, John Wiley&Sons (1994).
- [44] D.S. Watring, J.T. Benzing, N. Hrabe, A.D. Spear, Effects of laser-energy density and build orientation on the structure-property relationships in as-built inconel 718 manufactured by laser powder bed fusion, Addit. Manuf. 36 (2020) 101425.
- [45] L.-A. Liew, D.T. Read, M.L. Martin, F.W. DelRio, P.E. Bradley, N. Barbosa, T.R. Christenson, J.T. Geany, Elastic-plastic properties of mesoscale electrodeposited LIGA nickel alloy films: microscopy and mechanics, J. Micromech. Microeng. 31 (2021).
- [46] J.T. Benzing, L.-A. Liew, N. Hrabe, F.W. DelRio, Tracking defects and microstructural heterogeneities in meso-scale tensile specimens excised from additively manufactured parts, Exp Mech 60 (2) (2020) 165–170.
- [47] ASTM, E8-16a, Standard test methods for tension testing of metallic materials, Standard, ASTM International, 2016.
- [48] ij-plugins/ijp-toolkit, 2016, (https://github.com/ij-plugins/ijp-toolkit/wiki/ 3D-IO). Accessed: 2021-03-23.
- [49] M.A. Groeber, M.A. Jackson, DREAM.3D: A digital representation environment for the analysis of microstructure in 3D, Integrating Materials and Manufacturing Innovation 3 (1) (2014) 5, doi:10.1186/2193-9772-3-5.
- [50] U. Ayachit, The paraview guide: a parallel visualization application, Kitware, Inc., 2015.
- [51] B.L. Welch, The generalization of student's' problem when several different population variances are involved, Biometrika 34 (1/2) (1947) 28–35.
- [52] B. Shahriari, K. Swersky, Z. Wang, R.P. Adams, N. De Freitas, Taking the human out of the loop: a review of Bayesian optimization, Proc. IEEE 104 (1) (2015) 148–175
- [53] K. Shiozawa, Y. Morii, S. Nishino, L. Lu, Subsurface crack initiation and propagation mechanism in high-strength steel in a very high cycle fatigue regime, Int J Fatigue 28 (11) (2006) 1521–1532.
- [54] G. Chai, The formation of subsurface non-defect fatigue crack origins, Int J Fatigue 28 (11) (2006) 1533–1539.
- [55] J.M. Hyzak, I.M. Bernstein, The effect of defects on the fatigue crack initiation process in two P/M superalloys: Part II. surface-subsurface transition, Metall. Trans. A 13 (1) (1982) 45–52.
- [56] B.C. Salzbrenner, J.M. Rodelas, J.D. Madison, B.H. Jared, L.P. Swiler, Y.-L. Shen, B.L. Boyce, High-throughput stochastic tensile performance of additively manufactured stainless steel, J. Mater. Process. Technol. 241 (2017) 1–12.
- [57] Y. Kok, X.P. Tan, P. Wang, M. Nai, N.H. Loh, E. Liu, S.B. Tor, Anisotropy and heterogeneity of microstructure and mechanical properties in metal additive manufacturing: a critical review, Materials & Design 139 (2018) 565–586.